
This is an electronic reprint of the original article.
This reprint may differ from the original in pagination and typographic detail.

Horsten, N.; Groth, M.; Rikala, V. P.; Lomanowski, B.; Meigs, A. G.; Aleiferis, S.; Bonnin, X.; Corrigan, G.; Dekeyser, W.; Futtersack, R.; Harting, D.; Reiter, D.; Solokha, V.; Thomas, B.; Van den Kerkhof, S.; Vervloesem, N.; JET Contributors

Validation of SOLPS-ITER and EDGE2D-EIRENE simulations for H, D, and T JET ITER-like wall low-confinement mode plasmas

Published in:
Nuclear Materials and Energy

DOI:
[10.1016/j.nme.2024.101842](https://doi.org/10.1016/j.nme.2024.101842)

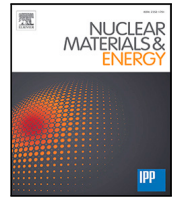
Published: 01/03/2025

Document Version
Publisher's PDF, also known as Version of record

Published under the following license:
CC BY-NC

Please cite the original version:
Horsten, N., Groth, M., Rikala, V. P., Lomanowski, B., Meigs, A. G., Aleiferis, S., Bonnin, X., Corrigan, G., Dekeyser, W., Futtersack, R., Harting, D., Reiter, D., Solokha, V., Thomas, B., Van den Kerkhof, S., Vervloesem, N., & JET Contributors (2025). Validation of SOLPS-ITER and EDGE2D-EIRENE simulations for H, D, and T JET ITER-like wall low-confinement mode plasmas. *Nuclear Materials and Energy*, 42, 1-12. Article 101842. <https://doi.org/10.1016/j.nme.2024.101842>

This material is protected by copyright and other intellectual property rights, and duplication or sale of all or part of any of the repository collections is not permitted, except that material may be duplicated by you for your research use or educational purposes in electronic or print form. You must obtain permission for any other use. Electronic or print copies may not be offered, whether for sale or otherwise to anyone who is not an authorised user.



Validation of SOLPS-ITER and EDGE2D-EIRENE simulations for H, D, and T JET ITER-like wall low-confinement mode plasmas

N. Horsten ^a, M. Groth ^b, V.-P. Rikala ^b, B. Lomanowski ^c, A.G. Meigs ^d, S. Aleiferis ^d, X. Bonnin ^e, G. Corrigan ^d, W. Dekeyser ^a, R. Futtersack ^d, D. Harting ^f, D. Reiter ^g, V. Solokha ^b, B. Thomas ^d, S. Van den Kerkhof ^a, N. Vervloesem ^a, JET Contributors ¹

^a KU Leuven, Department of Mechanical Engineering, Celestijnenlaan 300A, 3001 Leuven, Belgium

^b Department of Applied Physics, Aalto University, Espoo, Finland

^c Oak Ridge National Laboratory, Oak Ridge, TN, USA

^d UKAEA, Culham Science Centre, Abingdon, OX14 3DB, UK

^e ITER Organization, Route de Vinon-sur-Verdon, CS 90 046, F-13067, St-Paul-lez-Durance Cedex, France

^f Forschungszentrum Jülich, Institut für Energie- und Klimaforschung - Plasmaphysik, D-52425 Jülich, Germany

^g Institut für Laser- und Plasmaphysik, Heinrich-Heine-Universität, Düsseldorf, Germany

ARTICLE INFO

Keywords:

Plasma edge code validation
Divertor detachment
Lyman opacity
Balmer emission

ABSTRACT

Both experiments and simulations with SOLPS-ITER and EDGE2D-EIRENE show that the onset of detachment for the low-field side (LFS) divertor – defined here as the line-averaged upstream density $\langle n_e \rangle_{\text{edge}}$ at which the plasma flux to the LFS target ($I_{\text{LFS-plate}}$) starts to decrease with increasing $\langle n_e \rangle_{\text{edge}}$ – is independent of the isotope mass. However, there are three major simulation-experiment discrepancies: (i) the absolute values of $I_{\text{LFS-plate}}$ and the electron density (n_e) in the LFS divertor at the onset of detachment are significantly lower in simulations, i.e., approximately a factor of 2 for $I_{\text{LFS-plate}}$ and a factor of 3-4 for n_e ; (ii) the degree of detachment – defined here as the difference between $I_{\text{LFS-plate}}$ at the onset of detachment and at an $\langle n_e \rangle_{\text{edge}}$ value close to the density limit – is smaller in simulations compared to experiments; and (iii) the experimentally observed larger degree of detachment for D and T plasmas compared to H plasmas cannot be clearly distinguished from the simulation results. There are strong indications that discrepancy (i) is to a large extent caused by neglecting Lyman-opacity effects in our simulations. The simulations predict a similar net volumetric recombination source for all isotopes due to the fact that molecule-activated recombination (MAR) compensates for the reduced electron-ion recombination (EIR) for H, whereas MAR is negligible for D and T. This similar net volumetric recombination source for all isotopes leads to an isotope-independent degree of detachment in simulations. An analysis of the Balmer- α and Balmer- γ emission confirms the underestimate of MAR in simulations (especially for D and T) for the JET metallic wall, which was previously observed for devices with a carbon wall. The underestimate of MAR is an important cause for discrepancy (ii) and the fact that there is a stronger underestimate of MAR for D and T than for H explains discrepancy (iii). Extending the plasma grid to the vessel wall increases $I_{\text{LFS-plate}}$ and n_e at the onset of detachment by 25%, and the EIR source increases by 80% in detached conditions. Hence, while the extended grid results are closer to the experimental observations, the previously described qualitative discrepancies still persist.

1. Introduction

Detachment is the desired operating regime of a nuclear fusion reactor and is characterized by a strong reduction of the particle and energy fluxes to the divertor targets for a high upstream density, protecting them from eroding and melting. Hence, understanding the physics of

detachment is of crucial importance. This can be achieved through plasma edge modeling. Whereas future reactors are planned to operate with a deuterium (D) – tritium (T) mixture, most simulation models still assume pure D fuel, often supplemented with some minority impurity species. Only recently, significant progress has been made in modeling

* Corresponding author.

E-mail address: niels.horsten@kuleuven.be (N. Horsten).

¹ See the author list of “Overview of T and D-T results in JET with ITER-like wall” by CF Maggi et al. to be published in Nuclear Fusion Special Issue: Overview and Summary Papers from the 29th Fusion Energy Conference (London, UK, 16–21 October 2023).

D-T mixtures, see, e.g., Refs. [1–4]. Besides D and T, understanding the behavior of protium (H) is essential due to the frequent use of H during experimental campaigns of fusion devices. Consequently, it is essential to study the impact of isotope choice on several detachment characteristics. In this paper, we focus on two important detachment characteristics:

1. The onset of detachment, which we define as the minimum upstream density at which the divertor target particle flux starts to drop.
2. The degree of detachment, which we define as the total reduction of the target flux when further increasing the upstream density.

The divertor conditions are potentially impacted by many individual mass-dependent contributions. For the same energy, heavier ions are slower (the speed approximately scales with $1/\sqrt{m_{\text{ion}}}$, with m_{ion} the ion mass). The fast-reflected atoms and atoms resulting from molecular dissociation (with mass m_{at}) are slower for an increased mass. The pumping properties are affected by the mass of the molecule (m_{mol}), i.e., the conductance of the pump duct scales with $1/\sqrt{m_{\text{mol}}}$ and the sticking probability at the cryogenic panel increases with m_{mol} . In addition, the atom mean-free path scales with $1/\sqrt{m_{\text{at}}}$. There is an extended reaction database for cross sections and rate coefficients for H, but it is much more limited for D and T isotopes. Consequently, the H reaction database is typically used in simulations for all isotopes, but both the particle energy and background temperature for heavy particle collisions with D and T are rescaled with $m_{\text{H}}/m_{\text{D}}$ or $m_{\text{H}}/m_{\text{T}}$, where m_{H} , m_{D} , and m_{T} are the mass of an H, D, or T atom, respectively. This rescaling guarantees the same cross sections for collision partners with the same relative velocity difference. This effect should not be underestimated and will be discussed in detail in this paper.

JET has the unique capability to operate with different isotopes and isotope mixtures. The isotope effect on divertor conditions has already been studied for JET with a carbon wall (JET-C) [5]. For the JET ITER-like wall (JET-ILW), with beryllium main chamber and tungsten divertor, the characterization of detachment w.r.t. the effect of different isotopes has been done for Ohmic [6] and low-confinement mode (L-mode) [7] plasmas. The experimental analyses were supported by EDGE2D-EIRENE [8] simulations. However, there are still several important questions that remain unanswered, especially w.r.t. the validity of plasma edge codes for high-recycling and detached conditions. To this end, we further analyze the existing EDGE2D-EIRENE simulations and supplement them with SOLPS-ITER [9,10] simulations. SOLPS-ITER consists of the B2.5 code to solve fluid equations for the plasma species coupled to a kinetic Monte Carlo (MC) treatment for the neutrals with the EIRENE code [11]. The recently released extended grid version of SOLPS-ITER [12] allows extension of the plasma grid up to the real vessel wall, for which we will discuss the implications on the simulation results.

2. Experimental setup

We study pure H, D, and T JET-ILW L-mode plasmas with the high-field side (HFS) strike point at the vertical plate and the low-field side (LFS) strike point at the horizontal plate (Fig. 1). The plasma current and the toroidal magnetic field at the magnetic axis were 2.5 MA and 2.5 T, respectively, with the ion $\mathbf{B} \times \nabla B$ vector pointing into the divertor. There was 1 MW of neutral beam (NBI) heating power. The Ohmic heating power (P_{Ohm}) increases as a function of the upstream density, i.e., $P_{\text{Ohm}} \approx 1.5$ MW for low-recycling conditions and $P_{\text{Ohm}} \approx 2.2$ MW for detached conditions. The upstream density was controlled by means of a gas puff in the divertor (see Fig. 1), which was steadily increased during a discharge until the density limit was reached. Due to the continuous increase of the gas-puff strength in these ramping pulses, it might be that the plasma state is not responding fast enough to assume that it is in a (quasi) steady state for a certain

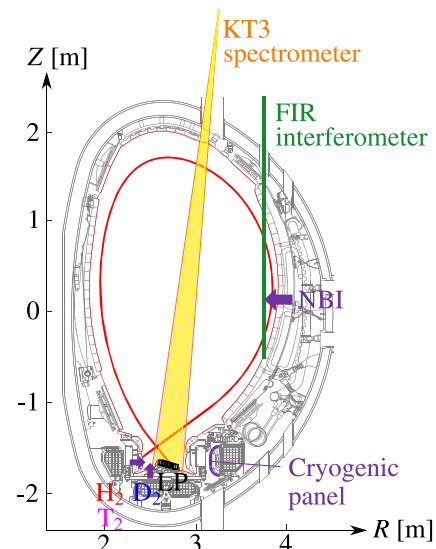


Fig. 1. Experimental setup. The diagnostics of interest are Langmuir probes (LPs), the KT3 spectrometer, and a far-infrared interferometer (FIR) to measure $\langle n_e \rangle_{\text{edge}}$. The yellow-shaded area corresponds to the tile-5 region over which the Balmer emission is averaged in Figs. 13–14, 21. Particles sticking at the cryogenic panel are pumped. (For interpretation of the references to color in this figure legend, the reader is referred to the web version of this article.)

Table 1

Overview of JET pulse numbers (JPNs).

JPN	Species	Cryogenic panel temperature
91 284	H	sc-He
94 759	D	sc-He
95 889	D	sc-He
100 166	T	LN ₂
100 559	D	LN ₂

puff strength. Because we assume a steady state for a certain puff strength in the simulations, we compared these ramping pulses with pulses where the puff strength was stepwise increased. We concluded that the transients of the plasma are fast enough to use the ramping pulses for a comparison with simulations.

Because of the maximum allowed throughput for T discharges, the cryogenic panel temperature for the T discharges was increased to liquid nitrogen temperatures (LN₂), whereas the panel for previous H and D discharges was operated at supercritical helium (sc-He) temperatures. The D pulse was also repeated for LN₂ settings (see Table 1) to assess the impact of the throughput on divertor conditions. For the remainder of the text, we often refer to the sc-He and LN₂ pulses as discharges with pumped and unpumped settings, respectively.

Because of its excellent diagnostic coverage, we focus on the LFS divertor in this paper. We use Langmuir probe (LP) data at the plate [13] for the plasma flux to the LFS divertor plate ($I_{\text{LFS-plate}}$) and line-integrated/-averaged measurements from the high-resolution poloidally scanning mirror spectrometer KT3 [14], as indicated in Fig. 1. The line-averaged electron density (n_e) and electron temperature (T_e) are inferred using Stark broadening of the Balmer- δ or Balmer- ϵ line and using the fitted continuum emission of the Balmer series, respectively [15,16]. LPs could be used to obtain T_e and n_e at the plate, but for $T_e < 10$ eV LPs become unreliable. As a result, Ref. [15] shows that LPs underestimate n_e in detached conditions with up to a factor of 3. Due to the focus in this paper on high-recycling and detached conditions and not to overload the figures, we only show the line-averaged n_e and T_e results from KT3 and we use LPs exclusively for the plasma particle flux. We study the divertor plasma profiles as a function of the line-averaged upstream density $\langle n_e \rangle_{\text{edge}}$, measured with a far-infrared (FIR) interferometer [17]. We choose to use $\langle n_e \rangle_{\text{edge}}$ instead

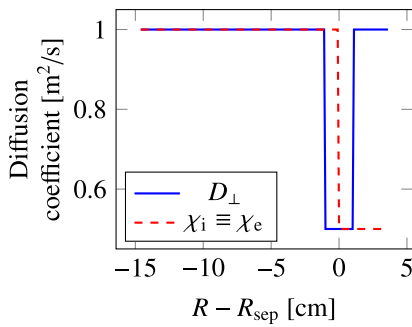


Fig. 2. Radial profiles of the particle (D_{\perp}) and thermal (χ_i and χ_e for the ions and electrons, respectively) diffusivities, where $R - R_{\text{sep}}$ corresponds to the radial distance from the separatrix at the OMP. Figure reproduced from Ref. [21], with permission.

of the more physics meaningful electron density at the outer-midplane (OMP) separatrix position ($n_{e,\text{sep},m}$), because obtaining $n_{e,\text{sep},m}$ is tedious due to uncertainties on the separatrix position and measurement errors. Ref. [18] derived the approximate relation $\langle n_e \rangle_{\text{edge}} \approx 2 \times n_{e,\text{sep},m}$ for the same JET L-mode configuration as this paper using the two-point model to estimate the shift of the measured profiles.

3. Simulation setup

Simulating mixtures of hydrogen isotopes leads to an increase of the statistical error by more than a factor 10^4 compared to simulations with a single isotope [4]. The reason is that the atom-ion charge-exchange reaction between different hydrogen species appears as a particle source/sink in the kinetic MC code EIRENE. Due to this statistical deterioration and due to the fact that D-T experimental results lie between the pure D and T results [7], we focus in this paper on simulations with pure H, D, or T.

The EDGE2D-EIRENE simulations also contain beryllium, but its impact on the plasma state was assessed to be small for D cases in high-recycling and detached conditions (beryllium accounts for approximately 15% of the total radiation in high-recycling and detached conditions [19]). Whereas there is a significant increase of the net erosion when transitioning from H to D, the differences between D and T are limited due to a smaller value for m_T/m_D than for m_D/m_H [20]. Consequently, we exclude beryllium from our SOLPS-ITER simulations to focus on the hydrogenic physics. In Section 4, we show that the impact of beryllium is indeed limited for the T EDGE2D-EIRENE cases.

Cross-field drifts and currents are activated in both EDGE2D-EIRENE and SOLPS-ITER. Neutral-neutral collisions are included in the SOLPS-ITER simulations, but their impact on the plasma state is limited, because the pressure in the sub-divertor entrances stays below 3 Pa. The perpendicular anomalous transport coefficients were manually tuned in Ref. [19] to fit the simulation results for n_e and T_e at the OMP location within the experimental uncertainties. This tuning was done for low-recycling conditions and the resulting transport coefficients are plotted in Fig. 2. We use the same transport coefficients for all our simulations. There are arguments to improve the transport coefficient values for high-recycling and detached conditions, which is out of the scope for this paper. Initial studies with variations of transport coefficients show that they impact the details of the divertor plasma profiles, but the effects on integrated quantities such as particle fluxes and radiation (the main quantities of interest of this paper) are small.

At the core-edge boundary (indicated in orange in Fig. 3), we impose a hydrogenic plasma particle flux of $8.5 \cdot 10^{19} \text{ s}^{-1}$ supplemented with a flux stemming from neutrals reaching the core region where they are ionized and re-enter the edge as fully stripped ions. These ionized neutrals typically dominate the plasma flux at the core-edge boundary. The power at the core-edge boundary (Q_{cor}) is assumed to be 2.2 MW, which is equally distributed between ions and electrons.

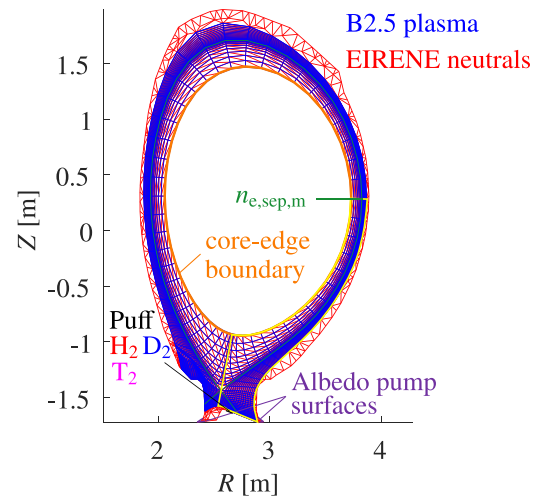


Fig. 3. SOLPS-ITER setup. The region indicated in yellow corresponds to the LFS region used in Sections 4–5 for the particle and energy balances. The sub-divertor entrances are blocked with pump surfaces with an albedo pump coefficient of 0.94. (For interpretation of the references to color in this figure legend, the reader is referred to the web version of this article.)

This power was estimated in Ref. [19] by subtracting the radiated power derived from the bolometric tomographic reconstructions from the total heating power. The increase in Ohmic power when increasing $\langle n_e \rangle_{\text{edge}}$ was observed to be approximately balanced by the increase in radiated power in the core. Hence, the 2.2 MW was assumed to be constant for all values of $\langle n_e \rangle_{\text{edge}}$. However, there are uncertainties on the input power, especially due to uncertainties on the tomographic reconstructions. In Section 4.2, we assess the impact of this uncertainty on the input power on the simulation results.

Finally, to mimic the experimental settings, there is a feedback gas puff in the simulations to control $n_{e,\text{sep},m}$, as shown in Fig. 3. The simulations are run for several values of $n_{e,\text{sep},m}$, each time until a statistically steady state is reached. Due to the Monte Carlo noise, the instantaneous residuals do not reach machine accuracy and only time-averaged quantities reach a steady state, which is the connotation of a “statically steady state”. The upstream density ranges from $n_{e,\text{sep},m} = 0.7 \cdot 10^{19} - 2.4 \cdot 10^{19} \text{ m}^{-3}$, where the upper limit corresponds to the approximate maximum density for which a stable solution is obtained. We use the $\langle n_e \rangle_{\text{edge}} \approx 2 \times n_{e,\text{sep},m}$ scaling from Ref. [18] to obtain $\langle n_e \rangle_{\text{edge}}$ for a comparison with the experiments. However, a future re-assessment of this relationship is recommended, as we will explain in this paper.

4. Validation for simulations with standard non-extended grids

The onset of detachment is independent of the isotope mass in both experiments and simulations (Fig. 4a). In Fig. 4 and upcoming figures, the following color code is used: red for H, blue for D, and magenta for T. For the $\langle n_e \rangle_{\text{edge}} = 2 \times n_{e,\text{sep},m}$ scaling, the roll-over of $I_{\text{LFS-plate}}$ occurs at similar upstream density in simulations as in experiments ($\langle n_e \rangle_{\text{edge}} \approx 2.6 \cdot 10^{19} \text{ m}^{-3}$). The LFS divertor line-averaged density rolls over at slightly higher $\langle n_e \rangle_{\text{edge}} \approx 3.0 \cdot 10^{19} \text{ m}^{-3}$ (Fig. 4b). The temperature at the $I_{\text{LFS-plate}}$ roll-over point is 2–3 eV and this temperature is reduced below 1 eV when further increasing $\langle n_e \rangle_{\text{edge}}$ (Fig. 4c). Although the experimental throughput in detached conditions is reduced with a factor 50 when increasing the cryogenic panel temperature from sc-He to LN₂, we do not observe a significant difference between pumped and unpumped conditions for these plasma profiles (compare the blue filled and open circles in Fig. 4a–b). The density limit is 20% higher for H plasmas, which is consistent with JET-C [5] and previous JET-ILW Ohmic/L-mode studies [6,7]. So, we conclude that $I_{\text{LFS-plate}}$ rolls over

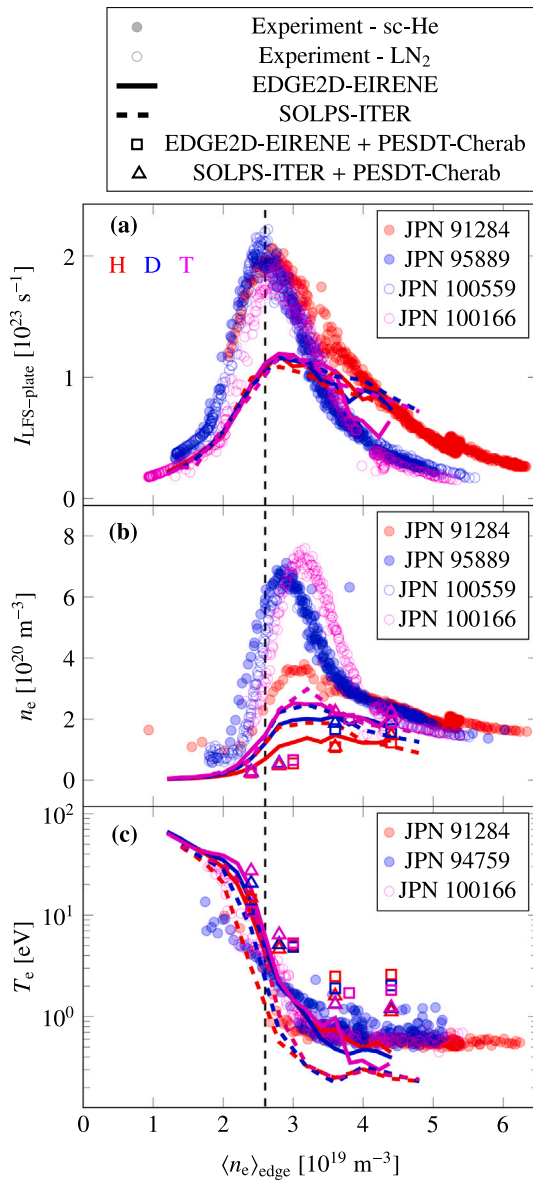


Fig. 4. LFS plate-integrated plasma current (a), electron density (b), and temperature (c). The current is measured with LPs and the experimental densities and temperatures are spectroscopically derived line-averaged quantities at the KT3 line of sight near the LFS strike point. The filled and open circles represent discharges with the cryogenic panel at sc-He and LN₂ temperatures, respectively. The lines indicate the maximum n_e at the LFS plate and T_e at the strike point from EDGE2D-EIRENE (solid) and SOLPS-ITER (dashed). The square and triangle symbols represent the line-averaged density and temperature calculated from the EDGE2D-EIRENE and SOLPS-ITER results with PESDT-Cherab. (For interpretation of the references to color in this figure legend, the reader is referred to the web version of this article.)

at the same upstream density for all isotopes and that this density is unaffected by the throughput.

This observation of an isotope-independent onset of detachment differs from what was previously concluded from JET-C studies. Fig. 9 of Ref. [5] shows for Ohmic plasmas a 20% decrease of the onset of detachment when moving from H to D. Ref. [6] concludes that for JET-ILW Ohmic plasmas the difference in onset of detachment between D and T remains below 10%, for both horizontal and vertical target configurations. With these Ohmic and our L-mode JET-ILW studies, we conclude that the isotope effect on carbon radiation played an important role for isotopic differences between the divertor target

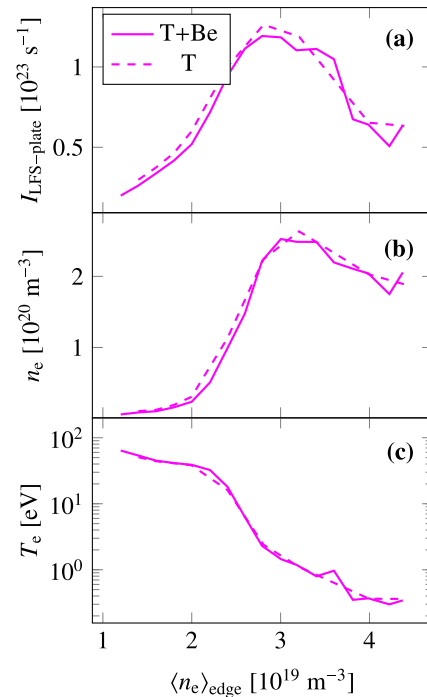


Fig. 5. Comparison between EDGE2D-EIRENE simulations with beryllium (solid lines) and without beryllium (dashed lines).

profiles for JET-C. The increased carbon radiation for heavier isotopes was also confirmed in Ref. [5].

There is no clear distinction between EDGE2D-EIRENE and SOLPS-ITER for $I_{\text{LFS-plate}}$ (solid versus dashed lines in Fig. 4a). The apparent lower value of $I_{\text{LFS-plate}}$ in detached conditions for T from EDGE2D-EIRENE is expected to be caused by deteriorated statistics. The EDGE2D-EIRENE simulations were already run previously and will be published in Ref. [22]. The EDGE2D-EIRENE simulations were run with ~ 10000 particles and EIRENE was only called once each ~ 10 EDGE2D time steps. Those are typical settings, because EDGE2D-EIRENE simulations are run on the JET computational machines with limited CPU resources and EDGE2D was only recently coupled to a parallelized EIRENE version. For SOLPS-ITER, we increased the number of particles to ~ 100000 and called EIRENE every B2.5 time step to improve the statistics. In addition, the SOLPS-ITER simulations are averaged over the last 1000 iterations. SOLPS-ITER predicts a slightly lower T_e in detachment compared to EDGE2D-EIRENE (0.25 eV versus 0.45 eV in Fig. 4c). This temperature reduction in SOLPS-ITER is compensated by a 25% increase of the peak density (Fig. 4b). These discrepancies are expected to be caused by differences in the formulation of the sheath boundary conditions. However, EDGE2D-EIRENE and SOLPS-ITER give qualitatively the same results and the code discrepancies are much smaller than the simulation-experiment discrepancies. A detailed code benchmark is out of scope for this paper.

To verify the assumption of a negligible effect of the beryllium radiation on the plasma profiles, we have rerun the EDGE2D-EIRENE T cases without beryllium. Fig. 5 shows that the beryllium impact is indeed small, and it is even smaller for the H and D cases due to the reduced beryllium sputtering.

The maximum value of n_e at the LFS target and T_e at the strike-point position are not fully equivalent to the line-averaged quantities inferred from spectroscopic measurements. A more fair comparison is made by post-processing the simulation results with the PESDT-Cherab tool [23,24] that calculates the line-averaged n_e from Stark broadening of the Balmer- δ line and the line-averaged T_e from the Balmer continuum emission, giving the synthetic equivalents of the

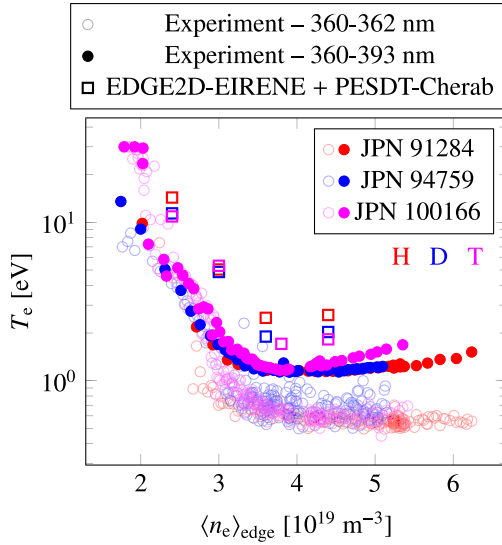


Fig. 6. Spectroscopically inferred line-averaged temperatures. The measurement results depend on the chosen wavelength range: 360–393 nm (filled circles) includes the recombination edge and 360–362 nm (open circles) is below the recombination edge.

measurements. The PESDT-Cherab results for the EDGE2D-EIRENE and SOLPS-ITER cases are indicated with respectively square and triangle symbols in Fig. 4b–c. The PESDT-Cherab analyses indicate that the density at the onset of detachment in simulations is underestimated with almost a factor of 4. Similar to the peak density increase, SOLPS-ITER predicts a 25% larger line-averaged density than EDGE2D-EIRENE in detached conditions. The line-averaged T_e from simulations does not get reduced below 1 eV and is to that extent closer to the upper estimate in experiments, obtained with a continuum wavelength range from 360–393 nm, i.e., the recombination edge is included (see Fig. 6). From these PESDT-Cherab post-processed results, we conclude that simulations underestimate n_e even more than what was previously observed by taking the maximum values at the LFS plate.

In general, there are three major simulation-experiment discrepancies:

1. Simulations underestimate $I_{\text{LFS-plate}}$ at the onset of detachment with approximately a factor of 2 and the density with more than a factor of 3.
2. In experiments, a larger degree of detachment is observed for D and T plasmas compared to H, i.e., $I_{\text{LFS-plate}}$ is lower for D and T than for H for the same value of $\langle n_e \rangle_{\text{edge}}$ after the roll-over. This isotopic differentiation cannot be distinguished from the simulation results.
3. The drop of $I_{\text{LFS-plate}}$ after the roll-over is larger in experiments compared to simulations implying a general larger degree of detachment in experiments.

In the remainder of Section 4, we explain the possible origin of these simulation-experiment discrepancies. Section 4.1 summarizes the theoretical background to understand the behavior of the target plasma particle flux. With this theory, we explain the possible origin of discrepancy 1 in Section 4.2. Section 4.3 deals with discrepancies 2–3. As the EDGE2D-EIRENE interpretations will be submitted elsewhere [22], we focus on the SOLPS-ITER results in the remainder of the text.

4.1. Theoretical background to estimate the divertor target flux

To obtain an expression for $I_{\text{LFS-plate}}$ as a function of $\langle n_e \rangle_{\text{edge}}$, we investigate the particle and energy balance. Similar to Ref. [25], the derivation is done for the entire plasma edge domain and Γ_w corresponds to the hydrogenic plasma flux to the entire plasma edge

boundary (excluding the core-edge boundary), i.e., the main chamber and the divertor targets. The derivations are easily adapted to get an expression for $I_{\text{LFS-plate}}$ by isolating the LFS region and assuming that the major part of the particle and energy flux is reaching the LFS target and not the main chamber wall. In that case, only the fraction of the plasma power reaching the LFS SOL has to be taken into account instead of the power reaching the entire scrape-off layer (SOL) (Q_{SOL}).

The particle and energy balance are expressed as

$$\Gamma_w \approx S_{\text{ion}} - S_{\text{rec}}, \quad (1)$$

$$Q_w \approx \gamma T_w \Gamma_w \\ \approx Q_{\text{SOL}} - E_{\text{ion}}^{\text{eff}} S_{\text{ion}} - Q_{\text{imp}}, \quad (2)$$

respectively, with S_{ion} and S_{rec} the volumetrically integrated ionization and recombination particle source, respectively. Eq. (1) is valid, because the hydrogenic ion particle flux entering the edge region from the core is much smaller than the recycling flux. This assumption is valid for our simulations, because at the onset of detachment ($\langle n_e \rangle_{\text{edge}} \approx 1.3 \cdot 10^{19} \text{ m}^{-3}$), the flux from the core (Γ_{core}) is of the order 10^{21} s^{-1} , whereas $I_{\text{LFS-plate}} \sim 10^{23} \text{ s}^{-1}$, and Γ_{core} further decreases for detached conditions. The first line of Eq. (2) gives the sheath boundary condition with γ the sheath energy transmission coefficient ($\gamma \approx 8.5$ for EDGE2D-EIRENE and SOLPS-ITER, where we assume that the macroscopic kinetic energy is included in the energy balance) and T_w a representative plasma temperature at the wall. The plasma power reaching the wall (Q_w) is determined by Q_{SOL} minus the hydrogenic energy losses and energy losses due to impurities (Q_{imp}). The impurity energy losses are included in the derivations to assess their possible impact, but neglected in the SOLPS-ITER simulations. The hydrogenic energy losses approximately scale with the ionization source, which explains that we approximate them as $-E_{\text{ion}}^{\text{eff}} S_{\text{ion}}$ in Eq. (2). Generally, the effective ionization energy ($E_{\text{ion}}^{\text{eff}}$) contains the electron energy losses due to ionization of hydrogenic atoms and molecules, dissociation of molecules, and radiation losses and ion energy sources/sinks due to plasma-neutral interactions (e.g., the creation of ions in ionization events and charge-exchange and elastic collisions). This energy loss term is almost fully determined by electron energy losses for high-recycling and detached conditions (see Section 4.2). It should be noted that Q_w is the plasma power to the wall and not the effective heat load. For the latter, the released energy during the surface recombination process and the surface interactions of neutrals and photons are added.

Combining Eqs. (1)–(2) gives an expression for the integrated particle flux to the wall:

$$\Gamma_w \approx \frac{Q_{\text{SOL}} - Q_{\text{imp}}}{E_{\text{ion}}^{\text{eff}} + \gamma T_w} - \frac{E_{\text{ion}}^{\text{eff}}}{E_{\text{ion}}^{\text{eff}} + \gamma T_w} S_{\text{rec}} \\ \approx \frac{Q_{\text{SOL}} - Q_{\text{imp}}}{E_{\text{ion}}^{\text{eff}} + \gamma T_w} - S_{\text{rec}}, \quad (3)$$

using the assumption that $E_{\text{ion}}^{\text{eff}} \gg \gamma T_w$ for temperatures where volumetric recombination plays an important role ($T_w \lesssim 1 \text{ eV}$). Eq. (3) corresponds to the closed-box approximation of Ref. [26] to study the roll-over of the plasma flux to the plasma-facing components. In Ref. [19], EDGE2D-EIRENE simulations show that for a D fuel the beryllium radiation in the edge is approximately 0.1 MW for high-recycling and detached conditions (compared to $Q_{\text{core}} = 2.2 \text{ MW}$) and the tungsten radiation becomes negligible. Hence, the impact of Q_{imp} in Eq. (3) is neglected in the upcoming analyses, which is justified in Fig. 5. With the help of Eq. (3), we will now explain the simulation-experiment discrepancies at the onset of detachment (Section 4.2) and in detached conditions (Section 4.3).

4.2. Underestimate of peak $I_{\text{LFS-plate}}$ and n_e in simulations

The maximum value of Γ_w as a function of $\langle n_e \rangle_{\text{edge}}$ is approximated by $Q_{\text{SOL}} / (E_{\text{ion}}^{\text{eff}} + \gamma T_w)$, which shows the linear scaling with Q_{SOL} . There are significant uncertainties on the power radiated in the core region

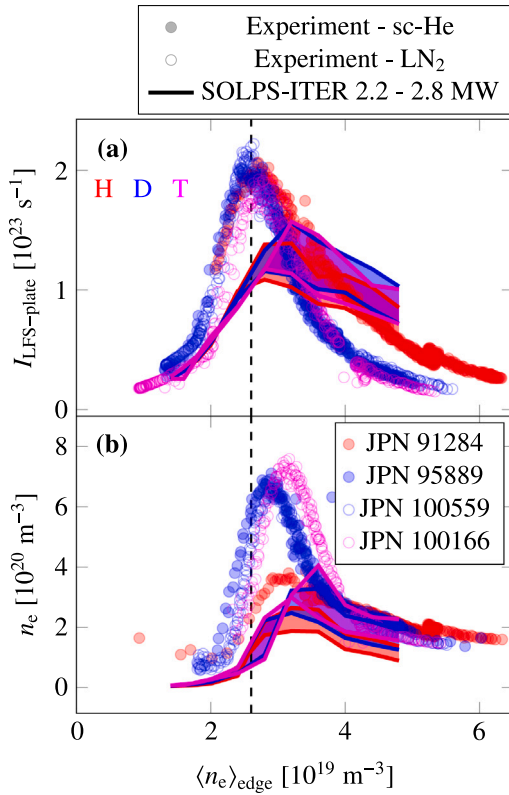


Fig. 7. Effect of varying the input power on $I_{\text{LFS-plate}}$ (a) and the maximum electron density at the LFS target (b) as a function of $\langle n_e \rangle_{\text{edge}}$ in SOLPS-ITER simulations.

(integrated from the center of the core to the core–edge boundary of the plasma grid) due to uncertainties on tomographic reconstructions of bolometric measurements. The originally assumed $Q_{\text{core}} = 2.2$ MW is estimated to be a lower limit. The upper limit is 2.8 MW. Increasing the power raises the peak $I_{\text{LFS-plate}}$ and n_e . However, simulations still underestimate $I_{\text{LFS-plate}}$ by at least 25% and n_e by at least 25%–50% (Fig. 7). The onset of detachment occurs at higher $\langle n_e \rangle_{\text{edge}}$ when increasing the power. Increasing Q_{core} from 2.2 MW to 2.8 MW leads to an increase of the electron temperature at the OMP separatrix position from approximately 60 eV to approximately 70 eV at the original onset of detachment ($n_{e,\text{sep,m}} = 1.3 \cdot 10^{19} \text{ m}^{-3}$). This temperature variation impacts the pressure balance. Due to the large sensitivities of simulation results w.r.t. the upstream pressure, it is essential to match the OMP separatrix pressure with experimental measurements for a one-on-one comparison of the divertor profiles for a certain value of $\langle n_e \rangle_{\text{edge}}$. Nevertheless, the uncertainties on Q_{core} are insufficient to explain the large differences between the peak values of $I_{\text{LFS-plate}}$ in simulations and experiments.

A critical factor in determining the peak value of $I_{\text{LFS-plate}}$ is the effective ionization energy $E_{\text{ion}}^{\text{eff}}$, which we define as

$$E_{\text{ion}}^{\text{eff}} \stackrel{\Delta}{=} -\frac{S_{E_e} + S_{E_i}}{S_{\text{ion}}}, \quad (4)$$

with S_{E_e} and S_{E_i} the integrated electron and ion energy source (including internal and macroscopic kinetic energy), respectively. Since there are no impurities in the SOLPS-ITER simulations, S_{E_e} and S_{E_i} are entirely determined by hydrogenic processes. Because of the focus in this paper on the LFS region, we integrate the particle and energy sources over the LFS region indicated in yellow in Fig. 3. We assume that the ionization source S_{ion} is fully determined by atom–electron ionization ($\mathbf{H} + e \rightarrow \mathbf{H}^+ + 2e$, where we use boldface \mathbf{H} here and for the remainder of the paper to denote any hydrogen isotope). Molecular processes also

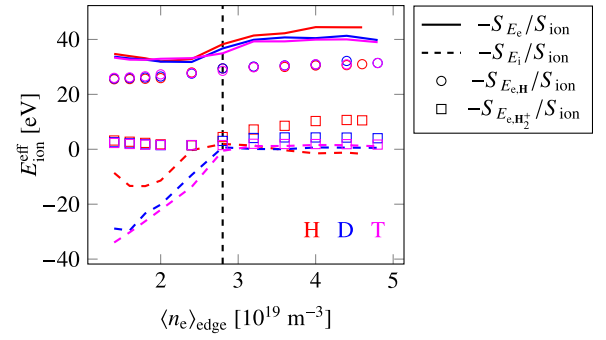


Fig. 8. Contributions of electron and ion energy sources to $E_{\text{ion}}^{\text{eff}}$ in SOLPS-ITER ($Q_{\text{core}} = 2.2$ MW), integrated over the LFS region indicated in yellow in Fig. 3. The vertical dashed line indicates the onset of detachment.

potentially lead to the production of \mathbf{H}^+ , but because this molecule-activated ionization (MAI) process competes with molecule-activated recombination (MAR), we assume that S_{rec} in Eq. (3) also contains the net recombination from molecular processes (see Section 4.3).

The contribution of S_{E_e} to $E_{\text{ion}}^{\text{eff}}$ for higher $\langle n_e \rangle_{\text{edge}}$ values than the onset of detachment is slightly larger for H compared to D and T (solid lines in Fig. 8) (~ 45 eV for H versus ~ 40 eV for D and T). This isotope effect is caused by the increased \mathbf{H}_2^+ density for H in the simulations. Reactions between \mathbf{H}_2^+ and electrons lead to increased electron energy losses. The \mathbf{H}_2^+ contribution (S_{E_e,\mathbf{H}_2^+}) is indicated with squares. The larger \mathbf{H}_2^+ density for H than for D and T plays an important role for the recombination source and we come back to that observation at the end of Section 4.3. The electron energy losses due to atom–electron interactions ($S_{E_e,\mathbf{H}}$) are similar for all isotopes (~ 30 eV), as indicated with circles. The ion energy source for low-recycling conditions is almost fully determined by atom–electron ionization, leading to a negative contribution to $E_{\text{ion}}^{\text{eff}}$. The reduced ionization mean-free path for heavier atoms increases the probability for ionization of D and T atoms in the edge before reaching the core region. Consequently, S_{E_i} increases for D and T plasmas. After the onset of detachment, S_{E_i} becomes negligible compared to S_{E_e} indicating the limited effectiveness of (in)elastic plasma–atom and plasma–molecule collisions as an energy sink. The effective ionization energy is similar for all isotopes at the onset of detachment, which leads to similar values of $I_{\text{LFS-plate}}$ (see Fig. 4a).

Including Lyman-opacity effects has a significant impact on the value of $E_{\text{ion}}^{\text{eff}}$ [27]. Properly taking into account Lyman opacity requires coupled plasma–neutral–photon simulations. The photon transport module in EIRENE was originally developed in Ref. [28] and is being revived in Ref. [29]. Instead of including photon transport, we estimate the upper limit of $I_{\text{LFS-plate}}$ and n_e due to Lyman opacity by repeating the SOLPS-ITER simulations for D using reaction 2.1.5o from the AMJUEL database [30] for the $\mathbf{H} + e \rightarrow \mathbf{H}^+ + 2e$ ionization reaction. In contrast to the original reaction 2.1.5 that assumes local escape factors of 1 for all Lyman emission lines (i.e., fully transparent), reaction 2.1.5o assumes zero escape factors (i.e., fully opaque). Fig. 9 shows that there is a 65% increase of the peak $I_{\text{LFS-plate}}$ and a factor 2.8 increase of the maximum electron density at the LFS target when using the opaque rate coefficients. So even for the low input power ($Q_{\text{core}} = 2.2$ MW), the simulation–experiment discrepancies significantly decrease due to a strong reduction of $E_{\text{ion}}^{\text{eff}}$ (Fig. 9c). It should be emphasized that using the Lyman-opaque rate coefficients leads to unrealistic plasma profiles in regions with low opacity (e.g., the OMP region) and this spatial dependence of the Lyman escape factors has to be taken into account in the future by means of consistent photon transport [29]. The adaptation of the rate coefficients should be accompanied with a re-assessment of the assumed $\langle n_e \rangle_{\text{edge}} - n_{e,\text{sep,m}}$ relation. The impact of Lyman opacity

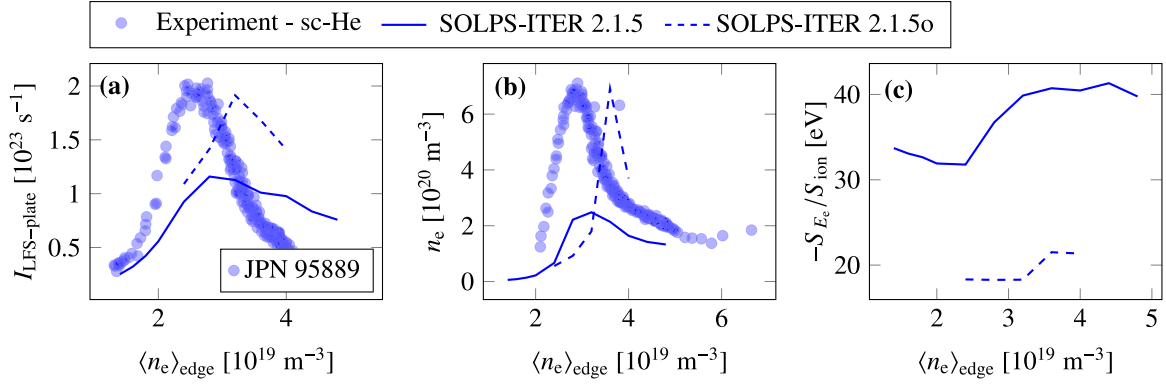


Fig. 9. Comparison of D SOLPS-ITER simulations ($Q_{\text{core}} = 2.2$ MW) with AMJUEL Lyman-opaque ionization rate coefficient (reaction 2.1.5o) and the standard transparent rate coefficient (reaction 2.1.5).

on $E_{\text{ion}}^{\text{eff}}$ seems to be a plausible explanation for the mismatch between simulations and experiments for the peak values of $I_{\text{LFS-plate}}$.

Although Ref. [31] reports that including photon transport has a negligible effect on the plasma state for JET-C simulations, there are strong experimental indications for the importance of Lyman opacity for JET-ILW plasmas [32,33]. Ref. [32] concludes that the Lyman- α reabsorption increases from 70% to 90%–98% when changing the wall material for JET from C to Be-W due to the larger atom density at the onset of detachment. Figs. 7–8 of Ref. [21] show that simulations underestimate the Balmer- α emission at the onset of detachment with a factor 2, whereas they overestimate the Lyman- α emission with a factor 2. From these observations, we recommend to reconsider photon transport calculations for metallic devices.

4.3. Study of recombination processes to reduce $I_{\text{LFS-plate}}$

Volumetric recombination directly reduces the plasma flux to the wall (see Eq. (3)). There are two categories of recombination processes:

1. Electron-ion recombination (EIR), which consists of three-body recombination ($\text{H}^+ + 2e \rightarrow \text{H} + e$) and radiative recombination ($\text{H}^+ + e \rightarrow \text{H} + \text{photon}$). The former process is dominant for temperatures below 1 eV.
2. Molecule-activated recombination (MAR). There are two mechanisms for MAR, each existing of two reaction steps:



and



The MAR process via H_2^+ (reaction chain (5)) can be considered as a recombination process that already becomes relevant at temperatures around 2 eV and is included in our simulations. We exclude the MAR process via H^- (reaction chain (6)) in our studies due to the strong isotope effect for that process, which is not properly taken into account by the commonly available reaction data. H^- has been excluded in the majority of plasma edge simulations due to the assumption that it is negligible for tokamak-relevant D and T plasmas. More recent work indicates that this assumption might need to be revisited [34], although also in that reference the isotope effect on D^- or T^- production via the dissociative attachment channels was not properly taken into account. A detailed study of the effect of H^- is beyond the scope of this paper.

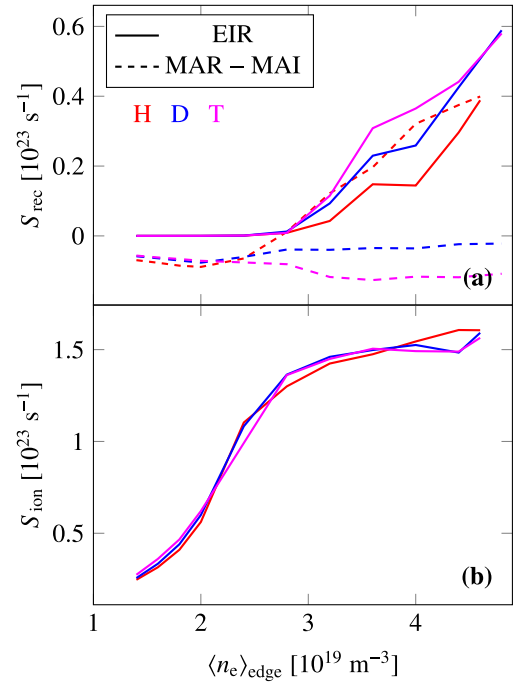


Fig. 10. Contributions to total recombination source (a) and ionization source (b) in LFS region (indicated in yellow in Fig. 3) in SOLPS-ITER ($Q_{\text{core}} = 2.2$ MW).

It should be noted that there are also competing molecule-activated ionization (MAI) processes and the net production of H atoms from molecular processes is evaluated as MAR - MAI. Both EIR and MAR processes are able to reduce $I_{\text{LFS-plate}}$ and we will study both processes in the next paragraphs.

In the simulations, D and T plasmas lead to 45% more EIR (solid lines in Fig. 10a). The increase in EIR for heavier isotopes is caused by the reduced velocity, which leads to longer dwell times in the SOL increasing the probability for recombination (Fig. 11a). The increased size of the region with $T_e < 1$ eV for H plasmas (Fig. 11b) in simulations is caused by the increased $E_{\text{ion}}^{\text{eff}}$ (Fig. 8) and makes the difference between the EIR source from different isotopes less strong than the expected $\sqrt{m_{\text{ion}}}$ scaling. Fig. 11a also shows that there is a strong reduction of the parallel velocity before the acceleration to the speed of sound due to large momentum losses. If only EIR recombination processes would be considered, there would indeed be a larger degree of detachment for D and T plasmas than for H plasmas.

However, also MAR processes can play an important role. In the simulations, there is only a net H production due to molecular processes

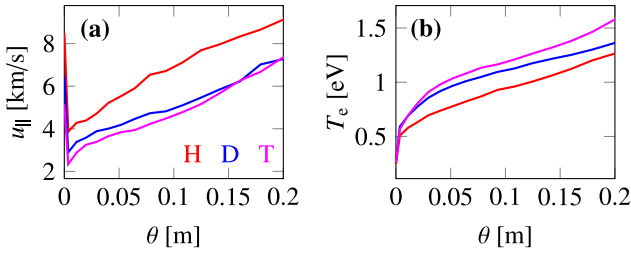


Fig. 11. Parallel plasma velocity (a) and electron temperature (b) in the first flux tube in the SOL adjacent to the separatrix as a function of the poloidal distance from the LFS target (θ) for SOLPS-ITER simulations with $\langle n_e \rangle_{\text{edge}} = 4.4 \text{ m}^{-3}$.

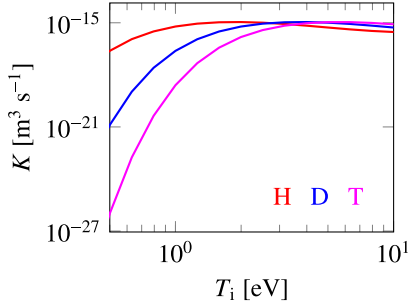


Fig. 12. Rate coefficient for $\text{H}_2 + \text{H}^+ \rightarrow \text{H}_2^+ + \text{H}$ reaction (AMJUEL 3.2.3) as a function of the ion temperature (T_i). An H_2 particle energy of $3T_i/2$ is assumed for the evaluation of the rate coefficients.

for H plasmas (dashed lines in Fig. 10a). The reason is that the mass rescaling in EIRENE leads to a reduction of the rate coefficient (K) for the $\text{H}_2 + \text{H}^+ \rightarrow \text{H}_2^+ + \text{H}$ charge-exchange reaction with orders of magnitude for D and T for temperatures below 1 eV (see Fig. 12). The net volumetric recombination source (EIR + MAR – MAI) is similar for all isotopes (only slightly larger for H), which leads to a similar reduction of $I_{\text{LFS-plate}}$ for all isotopes, because the slight increase in the net recombination source for H is compensated by a slight increase of the integrated atomic ionization source (Fig. 10b).

The experimental importance of different recombination processes is assessed by a Balmer emission analysis. SOLPS-ITER underestimates the Balmer- α and Balmer- γ emission in detached conditions with a factor 3–5 and 1.5–2, respectively (Fig. 13). It should be noted that the synthetic diagnostics from SOLPS-ITER do not account for the contributions of the reflected light, which can be up to 30%–40% of the measured emission for these JET-ILW plasmas [35]. However, this missing line emission does not explain the simulation-experiment discrepancies. The differences between pumped and unpumped conditions in Fig. 13 (blue filled and open circles, respectively) indicate a significant impact of the throughput on the Balmer emission, which is discussed in more detail in Ref. [36]. Comparing the measured emission for H and D plasmas with the cryogenic panel at sc-He temperatures (red versus blue filled circles) shows that the Balmer- α emission is larger for D than H. The opposite trend is observed in simulations. To understand the difference in trend between simulations and experiments, we study the different components of the Balmer emission.

H_2^+ contributes 50% of the total Balmer- α emission for simulations with H plasmas (red dashed line in Fig. 14). In contrast, the H_2^+ contribution is unimportant for D and T plasmas, which is consistent with the negligible MAR in simulations of D and T plasmas (Fig. 10a). The fact that the Balmer- α emission in simulations is larger for H than for D and T due to the H_2^+ contribution, which is opposite to experimental observations, is a strong indication that simulations underestimate the importance of MAR and that the reaction data for molecular processes has to be revisited, especially for D and T plasmas. This expected

stronger MAR recombination for D and T would bring the $I_{\text{LFS-plate}}$ values in detachment below the ones of H, which would be more in agreement with experimental observations. The underestimate of MAR in simulations was previously reported for the carbon devices TCV [37] and MAST-U [38] and is now also observed for the JET tungsten divertor. There is no isotope effect on the atom excitation component (circles in Fig. 14). The Balmer- γ emission is almost fully determined by the recombination (EIR) component. Finally, it is important to note that using AMJUEL reaction H.12 2.0c to calculate the H_2^+ density from the H_2 density (the standard way of calculating the emission in EIRENE) leads to a factor 4 overestimate of the Balmer- α emission for T plasmas. Hence, we conclude that AMJUEL reaction 2.0c, which was used to limit the statistical error on the H_2^+ density, can only be used for H plasmas.

A final note has to be made on the fact that the larger H_2^+ density for H than for D and T plasmas in simulations leads to an increase of $E_{\text{ion}}^{\text{eff}}$ in the detached regime, as shown in Fig. 8. This increase of $E_{\text{ion}}^{\text{eff}}$ further reduces $I_{\text{LFS-plate}}$ for H (see Eq. (3)) in contrast to experiments, which is an additional indication that plasma edge simulations are not correctly capturing the importance of MAR for D and T plasmas.

5. Impact of grid extension to the main chamber wall

Finally, we assess the impact of extending the plasma grid to the vessel wall by running SOLPS-ITER D simulations ($Q_{\text{core}} = 2.2 \text{ MW}$) on the grid of Fig. 15. The grid is optimized to minimize the discretization error [39]. Obtaining stable extended grid simulations with drifts and currents is still work in progress at the publication of these analyses. The numerical instabilities for drifts are caused by the triangular cells, which are introduced to match the vessel contour, in combination with a nine-point stencil. Current work focuses on for example the suppression of some nine-point contributions for the cross-field drifts. Because these adaptations are not yet available, we turn off the drifts and currents for both simulations on the extended grid and on the standard non-extended reference grid. At the end of this section, we also conclude that the effect of drifts does not alter the physics interpretations in this paper.

Extending the plasma grid increases the peak $I_{\text{LFS-plate}}$ and n_e by 25% (Fig. 16). The main increase of n_e and the ion saturation current density (j_{sat}) occurs in the SOL (Fig. 17). The larger $I_{\text{LFS-plate}}$ for the extended grid is not due to an increased target surface area, because the same target area as for the standard grid is used. For the extended grid, there is a 40% increase of the total plasma flux to the plasma grid boundary (excluding the core–edge boundary) (I_{tot}) in high-recycling and detached conditions (Fig. 18a). The factors in Eq. (3) for the wall flux that can be impacted by a grid extension are $E_{\text{ion}}^{\text{eff}}$ and T_w . Fig. 18b shows that $E_{\text{ion}}^{\text{eff}}$ is similar for both grids due to a similar composition of atoms and molecules.

The differences between standard and extended grid results are caused by the fundamentally different boundary conditions at the outermost flux surfaces. The original decay-length boundary conditions are now replaced by sheath boundary conditions, which leads to a redistribution of the plasma power (Fig. 19). The integrated plasma power going to the main chamber wall is reduced by almost 20% for the extended grid, which leads to an increase of available power to ionize the neutrals. Consequently, there is an increase of the ionization source (blue lines in Fig. 18c) and plasma particle flux to the targets. A similar effect can be achieved by tweaking the decay-length boundary conditions of the standard grid, but this is a tedious process due to missing measurements of the heat load on the main chamber wall. The extended grid eliminates the need of the decay-length (or alternatively leakage) parameters at the outermost flux surface. The spikes in Q for s_θ near 8 m are caused by the proximity of the sheath that accelerates the plasma.

For detached divertor conditions, there is an 80% increase of the recombination source when extending the grid (green lines in Fig. 18c).

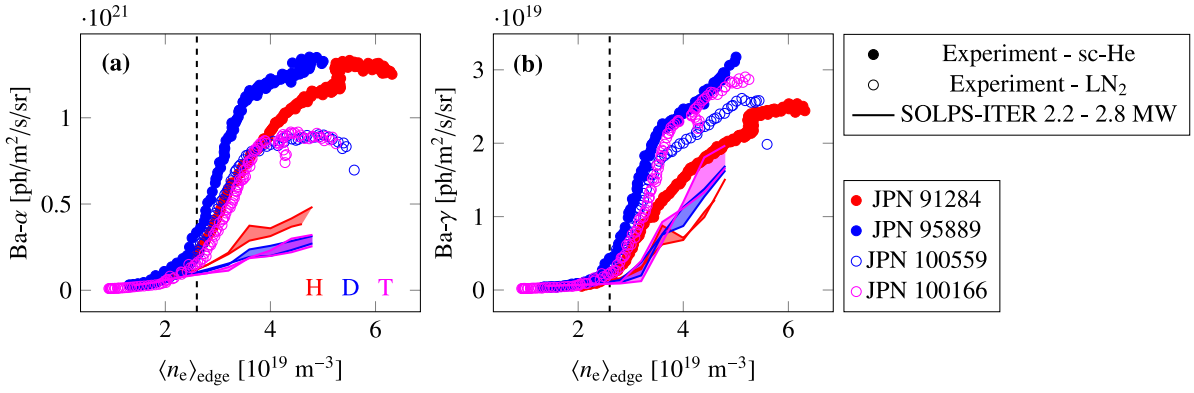


Fig. 13. Balmer- α (a) and Balmer- γ (b) emission averaged over tile 5 (yellow-shaded area in Fig. 1). The measurement data is coming from KT3e8Ta (Ba- α) and KT3e8Tb (Ba- γ), which utilize the lost light of KT3. The SOLPS-ITER simulations are run with $Q_{\text{core}} = 2.2$ MW and $Q_{\text{core}} = 2.8$ MW and the region in between is shaded. The vertical dashed line indicates the onset of detachment. (For interpretation of the references to color in this figure legend, the reader is referred to the web version of this article.)

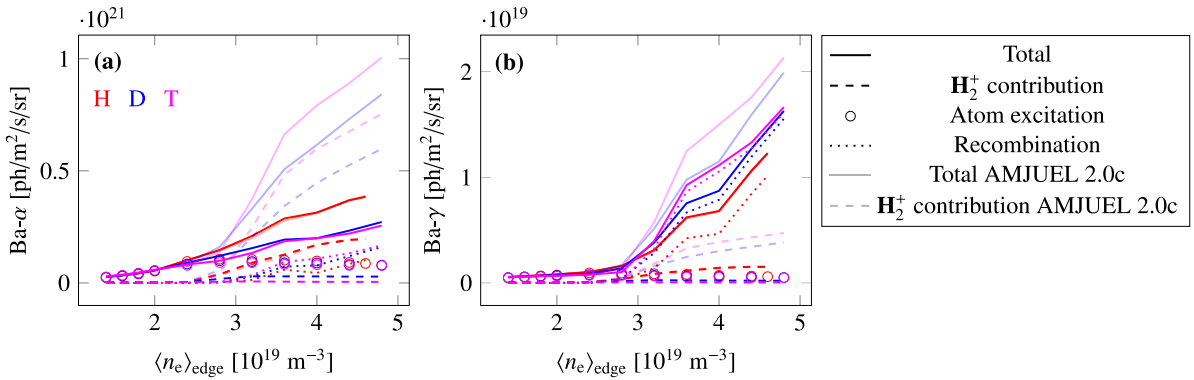


Fig. 14. Atomic and molecular contributions to the Balmer emission in SOLPS-ITER ($Q_{\text{core}} = 2.2$ MW). The non-transparent solid and dashed lines represent the emission obtained by directly using the H_2^+ density calculated in EIRENE. For the semi-transparent solid and dashed lines (the last two lines in the legend), the H_2^+ density to estimate the emission is recalculated from the EIRENE H_2 density using AMJUEL reaction H.12 2.0c. (For interpretation of the references to color in this figure legend, the reader is referred to the web version of this article.)

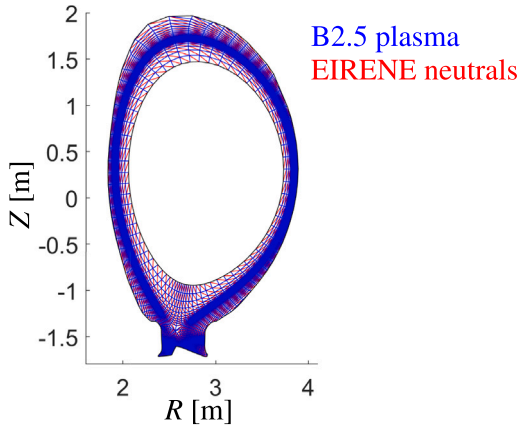


Fig. 15. Extended grid for which the B2.5 plasma grid now spans over the full EIRENE domain for neutrals.

This increase in recombination is caused by the increased density and not by the increased volume. Fig. 20 shows that the recombination peak in the SOL increases for the extended grid and that there is no significant recombination in the additional volume. The increased density leads to a 60% increase of the Balmer emission (Fig. 21). The experimental agreement of the Balmer- γ emission, which is mainly determined by EIR, significantly improves with the grid extension. The

Balmer- α emission from simulations remains much smaller than the experimental values due to the underestimate of MAR in simulations.

Finally, we conclude that the impact of drifts on the quantities of interest in this paper is limited for these L-mode plasmas. There is no observable difference between the simulation profiles of Fig. 4 and the standard grid results of Fig. 16. Drifts have an effect on the details of for example the target profiles, especially for low-recycling conditions, as discussed in Ref. [21]. The characteristics of detachment are barely affected by the presence of drifts.

6. Conclusions

The onset of detachment in the LFS divertor for the JET-ILW L-mode plasmas of this paper is independent of the isotope mass in both experiments and EDGE2D-EIRENE and SOLPS-ITER simulations. The simulations underestimate $I_{\text{LFS-plate}}$ and n_e in the LFS divertor at the onset of detachment with a factor of 2 and 3–4, respectively. These simulation-experiment discrepancies at the onset of detachment (for which volumetric recombination is still negligible) are mainly caused by uncertainties on the power crossing the core–edge boundary, the omission of Lyman-opacity effects in standard simulations, and not extending the plasma grid up to the main chamber wall giving artificial decay-length boundary conditions at the outermost flux surfaces instead of sheath boundary conditions at the entire wall. In detached conditions, the electron–ion recombination (EIR) increases for the heavier isotopes due to the increased dwell times in the low-temperature region near the target. This isotope effect on EIR is consistent with experiments where the Balmer- γ emission is larger for D and T than for H. In

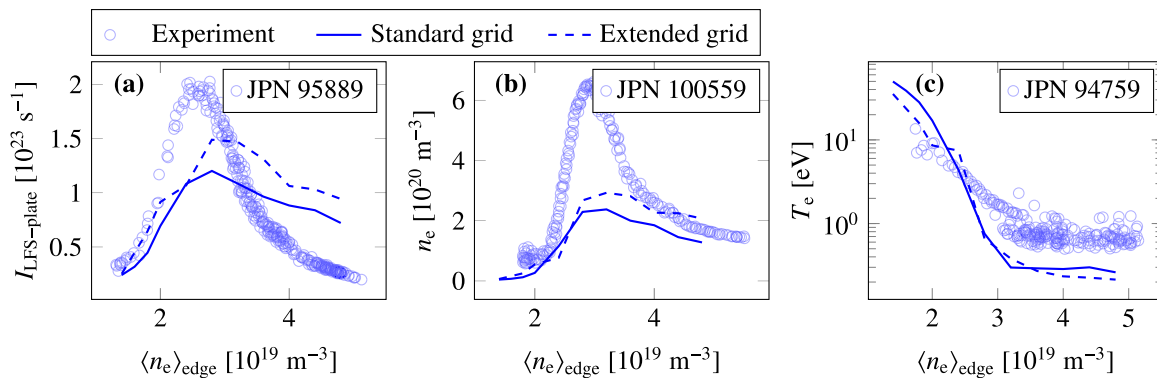


Fig. 16. Comparison of SOLPS-ITER D simulations with standard and extended grids. The experimental data for n_e and T_e are line-averaged spectroscopic measurements for the line of sight near the LFS strike point. The simulation plots represent the maximum electron density at the LFS target (b) and the electron temperature at the LFS strike point (c).

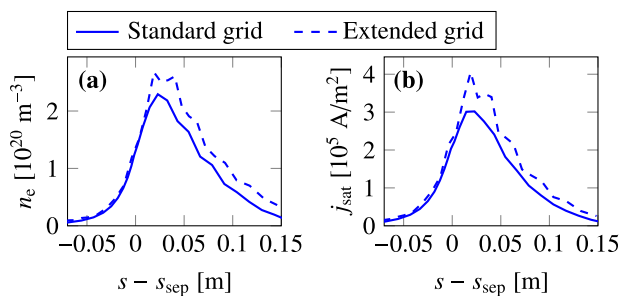


Fig. 17. Electron density (a) and ion saturation current density (b) at the LFS target as a function of the distance from the separatrix at the onset of detachment ($\langle n_e \rangle_{\text{edge}} = 2.8 \cdot 10^{19} \text{ m}^{-3}$).

simulations, molecule-activated recombination (MAR) contributes to 50% of the total recombination for H, but is completely negligible for D and T. From Balmer- α and Balmer- γ analyses, we conclude that MAR is also important for D and T in experiments. The underestimate of MAR in simulations is an important cause for the lower degree of detachment compared to experiments, at least for D and T plasmas.

Extending the plasma grid to the main chamber wall increases $I_{\text{LFS-plate}}$ and n_e at the LFS target at the onset of detachment with 25% and the Balmer emission with 60%. As future work, there is a need to perform increased-fidelity reference simulations by including photon transport [29] and either adding a collisional-radiative model for molecules (and possibly also including the effect of MAR via the H^- chain) or even tracking individual vibrationally excited states of molecules with revisited reaction data [40–42]. Including these physics features in computationally feasible simulations of current-day devices will give critical information to incorporate in design simulations of future reactors.

CRedit authorship contribution statement

N. Horsten: Writing – original draft, Visualization, Validation, Software, Methodology, Investigation, Formal analysis, Data curation, Conceptualization. **M. Groth:** Writing – review & editing, Validation, Supervision, Methodology, Investigation, Funding acquisition, Formal analysis, Conceptualization. **V.-P. Rikala:** Software, Methodology. **B. Lomanowski:** Software, Formal analysis. **A.G. Meigs:** Validation, Formal analysis. **S. Aleiferis:** Validation, Formal analysis. **X. Bonnin:** Writing – review & editing, Software. **G. Corrigan:** Software. **W. Dekeyser:** Writing – review & editing, Software. **R. Fattersack:** Software. **D. Harting:** Software. **D. Reiter:** Methodology. **V. Solokha:** Formal analysis. **B. Thomas:** Validation, Formal analysis. **S. Van den Kerkhof:** Software. **N. Vervloesem:** Software.

Table 2

Catalog numbers for EDGE2D-EIRENE simulations (username: mgroth; pulse number: 81472).

$n_{e,\text{sep,m}} [10^{19} \text{ m}^{-3}]$	H	D	T
0.7	sep0922/seq#1	jul3022/seq#1	sep0522/seq#1
0.8	sep1222/seq#1	jul3022/seq#2	aug2922/seq#2
0.9	sep0822/seq#1	jul3022/seq#3	aug2622/seq#1
1.0	aug1822/seq#1	aug0122/seq#1	aug1322/seq#1
1.2	aug2122/seq#2	jul3022/seq#4	aug2022/seq#2
1.4	aug2322/seq#1	jul3122/seq#1	aug2122/seq#4
1.6	aug2922/seq#1	aug0122/seq#3	sep0722/seq#1
1.8	sep1322/seq#1	aug0522/seq#3	oct0722/seq#1
2.0	sep1622/seq#1	aug0722/seq#1	aug2822/seq#2
2.2	sep1622/seq#3	aug0322/seq#3	aug2622/seq#2

Declaration of competing interest

The authors declare that they have no known competing financial interests or personal relationships that could have appeared to influence the work reported in this paper.

Acknowledgments

This work has been carried out within the framework of the EUROfusion Consortium, funded by the European Union via the Euratom Research and Training Programme (Grant Agreement No 101052200 — EUROfusion). Views and opinions expressed are however those of the author(s) only and do not necessarily reflect those of the European Union or the European Commission. Neither the European Union nor the European Commission can be held responsible for them. The views and opinions expressed herein do not necessarily reflect those of the ITER Organization. N. Horsten is a postdoctoral research fellow of the Research Foundation Flanders (FWO) under grant number 12AES24N. The computational resources and services used in this work were provided by the VSC (Flemish Supercomputer Center), funded by the Research Foundation Flanders (FWO) and the Flemish Government - department EWI.

Data availability

The EDGE2D-EIRENE simulations are cataloged at the JET Data Centre, see Table 2. The SOLPS-ITER results and setups can be downloaded from an open source online repository [43].

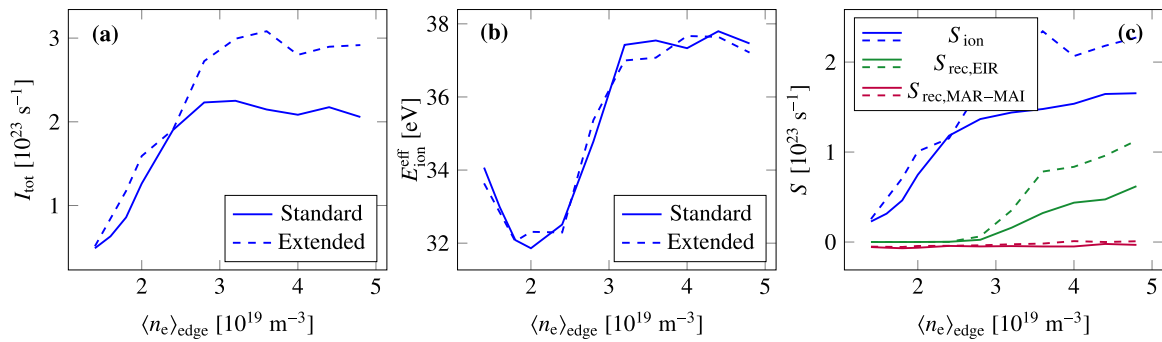


Fig. 18. Plasma flux to the entire plasma boundary (a), $E_{\text{ion}}^{\text{eff}}$ calculated with $-S_{E_e}/S_{\text{ion}}$ using the sources integrated over the whole plasma domain (b), and the particle balance in the LFS region indicated in yellow in Fig. 3(c). Standard grid (solid lines) and extended grid (dashed lines). (For interpretation of the references to color in this figure legend, the reader is referred to the web version of this article.)

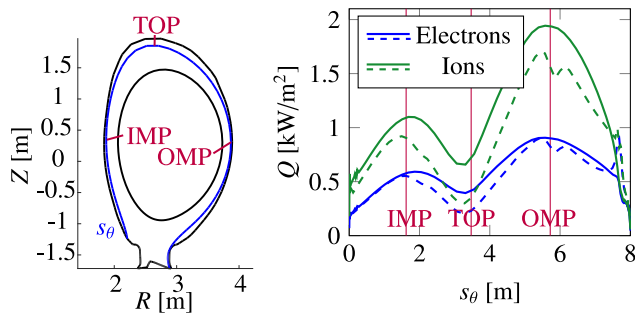


Fig. 19. Total electron and ion energy flux density through the outermost flux surface of the standard grid, indicated in blue on the left-hand side, as a function of the poloidal distance s_θ for $\langle n_e \rangle_{\text{edge}} = 2.8 \cdot 10^{19} \text{ m}^{-3}$. Standard grid (solid lines) and extended grid (dashed lines). (For interpretation of the references to color in this figure legend, the reader is referred to the web version of this article.)

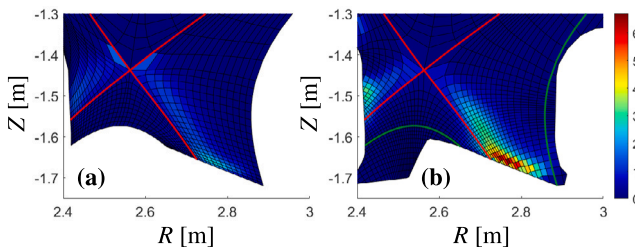


Fig. 20. Recombination source (EIR) $[10^{23} \text{ m}^{-3} \text{ s}^{-1}]$ for $\langle n_e \rangle_{\text{edge}} = 4.4 \cdot 10^{19} \text{ m}^{-3}$: standard grid (a) and extended grid (b). The green line in (b) corresponds to the boundary of the standard grid of (a). (For interpretation of the references to color in this figure legend, the reader is referred to the web version of this article.)

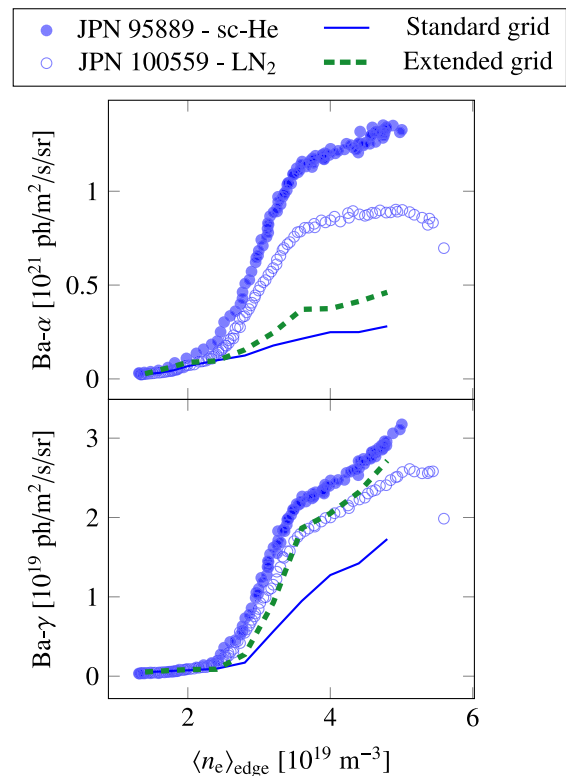


Fig. 21. Line-integrated Balmer- α (a) and Balmer- γ (b) emission averaged over tile 5 (see Fig. 1).

References

- [1] M. Raghunathan, Y. Marandet, H. Bufferand, G. Ciraolo, P. Ghendrih, P. Tamain, E. Serre, Multi-temperature generalized Zhdanov closure for scrape-off layer/edge applications, *Plasma Phys. Control. Fusion* 64 (4) (2022) 045005.
- [2] H. Bufferand, J. Balbin, S. Baschetti, J. Bucalossi, G. Ciraolo, P. Ghendrih, R. Mao, N. Rivals, P. Tamain, H. Yang, et al., Implementation of multi-component Zhdanov closure in SOLEDGE3X, *Plasma Phys. Control. Fusion* 64 (5) (2022) 055001.
- [3] S. Makarov, D. Coster, E. Kaveeva, V. Rozhansky, I. Senichenkov, I. Veselova, S. Voskoboinikov, A. Stepanenko, X. Bonnin, R. Pitts, Implementation of SOLPS-ITER code with new Grad-Zhdanov module for D-T mixture, *Nucl. Fusion* 63 (2) (2023) 026014.
- [4] E. Kaveeva, I. Veselova, V. Rozhansky, R.A. Pitts, V. Mikhailov, A. Zinoviev, Predictive modeling of the JET D-T plasma boundary, *Contrib. Plasma Phys.* (2023) e202300118.
- [5] C. Maggi, R. Monk, L. Horton, K. Borrass, G. Corrigan, L. Ingesson, R. König, G. Saibene, R. Smith, M. Stamp, et al., The isotope effect on the I mode density limit in JET hydrogen, deuterium and tritium divertor plasmas, *Nucl. Fusion* 39 (8) (1999) 979.

- [6] V. Solokha, M. Groth, S. Brezinsek, M. Brix, G. Corrigan, C. Guillemaut, D. Harting, S. Jachmich, U. Kruezi, S. Marsen, et al., The role of drifts on the isotope effect on divertor plasma detachment in JET ohmic discharges, *Nucl. Mater. Energy* 25 (2020) 100836.
- [7] M. Groth, V. Solokha, S. Aleiferis, S. Brezinsek, M. Brix, I. Carvalho, P. Carvalho, G. Corrigan, D. Harting, N. Horsten, et al., Characterisation of divertor detachment onset in JET-ILW hydrogen, deuterium, tritium and deuterium-tritium low-confinement mode plasmas, *Nucl. Mater. Energy* 34 (2023) 101345.
- [8] R. Simonini, G. Corrigan, G. Radford, J. Spence, A. Taroni, Models and numerics in the multi-fluid 2-D edge plasma code EDGE2D/U, *Contrib. Plasma Phys.* 34 (2-3) (1994) 368-373.
- [9] S. Wiesen, D. Reiter, V. Kotov, M. Baelmans, W. Dekeyser, A. Kukushkin, S. Lisgo, R. Pitts, V. Rozhansky, G. Saibene, et al., The new SOLPS-ITER code package, *J. Nucl. Mater.* 463 (2015) 480-484.
- [10] X. Bonnin, W. Dekeyser, R. Pitts, D. Coster, S. Voskoboinikov, S. Wiesen, Presentation of the new SOLPS-ITER code package for tokamak plasma edge modelling, *Plasma Fusion Res.* 11 (2016) 1403102-1403102.
- [11] D. Reiter, M. Baelmans, P. Börner, The EIRENE and B2-EIRENE codes, *Fusion Sci. Technol.* 47 (2) (2005) 172-186.

- [12] W. Dekeyser, P. Boerner, S. Voskoboinikov, V. Rozhankys, I. Senichenkov, L. Kaveeva, I. Veselova, E. Vekshina, X. Bonnin, R. Pitts, et al., Plasma edge simulations including realistic wall geometry with SOLPS-ITER, *Nucl. Mater. Energy* 27 (2021) 100999.
- [13] R. Monk, A. Loarte, A. Chanin, S. Clement, S. Davies, J. Ehrenberg, H. Guo, J. Lingertat, G. Matthews, M. Stamp, et al., Interpretation of ion flux and electron temperature profiles at the JET divertor target during high recycling and detached discharges, *J. Nucl. Mater.* 241 (1997) 396–401.
- [14] A. Meigs, M. Stamp, R. Igreja, S. Sanders, P. Heesterman, et al., Enhancement of JET's mirror-link near-ultraviolet to near-infrared divertor spectroscopy system, *Rev. Sci. Instrum.* 81 (10) (2010) 10E532.
- [15] A. Meigs, S. Brezinsek, M. Clever, A. Huber, S. Marsen, C. Nicholas, M. Stamp, K.-D. Zastrow, et al., Deuterium balmer/stark spectroscopy and impurity profiles: First results from mirror-link divertor spectroscopy system on the JET ITER-like wall, *J. Nucl. Mater.* 438 (2013) S607–S611.
- [16] B. Lomanowski, A. Meigs, R. Sharples, M. Stamp, C. Guillemaut, et al., Inferring divertor plasma properties from hydrogen balmer and paschen series spectroscopy in JET-ILW, *Nucl. Fusion* 55 (12) (2015) 123028.
- [17] A. Boboc, M. Gelfusa, A. Murari, P. Gaudio, et al., Recent developments of the JET far-infrared interferometer-polarimeter diagnostic, *Rev. Sci. Instrum.* 81 (10).
- [18] M. Groth, S. Brezinsek, P. Belo, G. Corrigan, D. Harting, S. Wiesen, M. Beurskens, M. Brix, M. Clever, J. Coenen, et al., Target particle and heat loads in low-triangularity L-mode plasmas in JET with carbon and beryllium/tungsten walls, *J. Nucl. Mater.* 438 (2013) S175–S179.
- [19] M. Groth, S. Brezinsek, P. Belo, M. Beurskens, M. Brix, M. Clever, J. Coenen, C. Corrigan, T. Eich, J. Flanagan, et al., Impact of carbon and tungsten as divertor materials on the scrape-off layer conditions in JET, *Nucl. Fusion* 53 (9) (2013) 093016.
- [20] J. Romazanov, A. Kirschner, S. Brezinsek, R. Pitts, D. Borodin, S. Rode, M. Navarro, K. Schmid, E. Veshchev, V. Neverov, et al., Beryllium erosion and redeposition in ITER H, He and D–T discharges, *Nucl. Fusion* 62 (3) (2022) 036011.
- [21] N. Horsten, M. Groth, W. Dekeyser, W. Van Uytven, S. Aleiferis, S. Carli, J. Karhunen, K. Lawson, B. Lomanowski, A. Meigs, et al., Validation of SOLPS-ITER simulations with kinetic, fluid, and hybrid neutral models for JET-ILW low-confinement mode plasmas, *Nucl. Mater. Energy* 33 (2022) 101247.
- [22] M. Groth, et al., Impact of H, D, T and D-T hydrogenic isotopes on detachment in JET ITER-like wall low-confinement mode plasmas, *Nucl. Fusion* (2024) in preparation.
- [23] B. Lomanowski, M. Carr, A. Field, M. Groth, A. Jaervinen, C. Lowry, A. Meigs, S. Menmuir, M. O'Mullane, M. Reinke, et al., Spectroscopic investigation of n and ne seeded induced detachment in JET ITER-like wall L-modes combining experiment and EDGE2D modeling, *Nucl. Mater. Energy* 20 (2019) 100676.
- [24] M. Carr, A. Meakins, A. Bacierno, M. Bernert, A. Callarelli, A. Field, C. Giroud, J. Harrison, N. Hawkes, S. Henderson, et al., Towards integrated data analysis of divertor diagnostics with ray-tracing, in: 44th EPS Conference on Plasma Physics, European Physical Society, 2017.
- [25] A. Pshenov, A. Kukushkin, S. Krasheninnikov, Energy balance in plasma detachment, *Nucl. Mater. Energy* 12 (2017) 948–952.
- [26] S. Krasheninnikov, A. Kukushkin, A. Pshenov, Divertor plasma detachment, *Phys. Plasmas* 23 (5).
- [27] A. Pshenov, A. Kukushkin, A. Gorbunov, E. Marenkov, Divertor plasma opacity effects, *Nucl. Mater. Energy* 34 (2023) 101342.
- [28] S. Wiesen, D. Reiter, P. Börner, H. Giese, M. Born, S. Meier, M. Baeva, Benchmarking the EIRENE divertor radiation transfer module using high pressure gas discharge lamps, in: Proceedings of 30th EPS Conference on Controlled Fusion and Plasma Physics.
- [29] R. Chandra, D. Reiter, N. Horsten, M. Groth, Lyman line opacities in tokamak divertor plasmas under high-recycling and detached conditions, *Nucl. Mater. Energy* 41 (2024) 101794.
- [30] D. Reiter, The Data File AMJUEL: Additional Atomic and Molecular Data for EIRENE, Tech. rep., FZ Juelich, 2000.
- [31] V. Kotov, D. Reiter, R.A. Pitts, S. Jachmich, A. Huber, D.P. Coster, et al., Numerical modelling of high density JET divertor plasma with the SOLPS4.2 (B2-EIRENE) code, *Plasma Phys. Control. Fusion* 50 (10) (2008) 105012.
- [32] B. Lomanowski, M. Groth, I. Coffey, J. Karhunen, C. Maggi, A. Meigs, S. Menmuir, M. O'Mullane, et al., Interpretation of Lyman opacity measurements in JET with the ITER-like wall using a particle balance approach, *Plasma Phys. Control. Fusion* 62 (6) (2020) 065006.
- [33] J. Karhunen, B. Lomanowski, S. Aleiferis, P. Carvalho, M. Groth, A. Holm, K. Lawson, A. Meigs, A. Shaw, V. Solokha, Addressing the impact of Lyman opacity in inference of divertor plasma conditions with 2D spectroscopic camera analysis of balmer emission during detachment in JET L-mode plasmas, *Nucl. Mater. Energy* (2024) submitted for publication.
- [34] A. Kukushkin, S. Krasheninnikov, A. Pshenov, D. Reiter, Role of molecular effects in divertor plasma recombination, *Nucl. Mater. Energy* 12 (2017) 984–988.
- [35] V.-P. Rikala, M. Groth, A. Meigs, B. Lomanowski, A. Shaw, S. Aleiferis, G. Corrigan, I. Carvalho, D. Harting, N. Horsten, I. Jezu, J. Karhunen, K. Lawson, C. Lowry, S. Menmuir, B. Thomas, D. Borodin, D. Douai, A. Huber, Characterization of detachment inferred from balmer line ratios in JET-ILW low-confinement mode plasmas, *Nucl. Mater. Energy* (2024) submitted for publication.
- [36] A. Meigs, M. Groth, V.-P. Rikala, B. Lomanowski, Balmer emission measurements in JET-ILW hydrogen, deuterium, tritium and deuterium-tritium low-confinement mode plasmas, *Nucl. Mater. Energy* (2024) submitted for publication.
- [37] K. Verhaegh, B. Lipschultz, J. Harrison, B. Duval, C. Bowman, A. Fil, D.S. Gahle, D. Moulton, O. Myatra, A. Perek, et al., A study of the influence of plasma-molecule interactions on particle balance during detachment, *Nucl. Mater. Energy* 26 (2021) 100922.
- [38] K. Verhaegh, B. Lipschultz, J. Harrison, F. Federici, D. Moulton, N. Lonigro, S. Kobussen, M.O. Mullane, N. Osborne, P. Ryan, et al., The role of plasma-atom and molecule interactions on power & particle balance during detachment on the MAST Upgrade Super-X divertor, *Nucl. Fusion* 63 (12) (2023) 126023.
- [39] N. Vervloesem, W. Dekeyser, S. van den Kerkhof, M. Baelmans, Error-based grid adaptation methods for plasma edge simulations with SOLPS-ITER, *Contrib. Plasma Phys.* (2024) e202300126.
- [40] D. Wunderlich, M. Giacomini, R. Ritz, U. Fantz, Yacora on the Web: Online collisional radiative models for plasmas containing H, H₂ or He, *J. Quant. Spectrosc. Radiat. Transfer* 240 (2020) 106695.
- [41] D.V. Borodin, F. Schluck, S. Wiesen, D. Harting, P. Boerner, S. Brezinsek, W. Dekeyser, S. Carli, M. Blommaert, W. Van Uytven, et al., Fluid, kinetic and hybrid approaches for neutral and trace ion edge transport modelling in fusion devices, *Nucl. Fusion* 62 (8) (2022) 086051.
- [42] J. Bryant, et al., Detachment onset in coupled Yacora-SOLPS-ITER simulations, *Nucl. Mater. Energy* (2024) submitted for publication.
- [43] N. Horsten, Replication data for: Validation of SOLPS-ITER and EDGE2d-EIRENE simulations for H, D, and T JET ITER-like wall low-confinement mode plasmas, 2024, <http://dx.doi.org/10.48804/WH90PQ>.